RSC Advances

PAPER

View Article Online
View Journal | View Issue

Check for updates

Cite this: *RSC Adv.*, 2025, **15**, 25322

Ce-doped nano-Fe–TiO_2 composites for photocatalytic degradation of naphthol blue black in aqueous medium†

Md. Burhan Kabir Suhan,[a] Md. Khairul Bahar[a] and Md. Shahinoor Islam *[ab]

In this study, the effectiveness of Ce-doped nano-Fe–TiO_2 composites as photocatalysts for the degradation of Naphthol Blue Black (NBB) dye present in water was investigated. Several TiO_2 nano-photocatalysts were synthesized using the sol–gel method, including undoped TiO_2, TiO_2 doped with Fe (TF), and co-doped with Fe_2O_3–CeO_2 (TFC), Fe_2O_3–Ag_2O (TFA), and Fe_2O_3–CeO_2–Ag_2O (TFCA). Characterizations of the synthesized catalysts were performed using Fourier Transform Infrared Spectroscopy (FTIR), X-ray Diffraction (XRD), and Scanning Electron Microscopy (SEM) to understand their structural and morphological properties. Photocatalytic performance was evaluated by measuring the degradation of NBB dye under ultraviolet (UV) light irradiation in a suspension configuration. The results demonstrated a significant enhancement in the light-absorption properties of TiO_2 nanoparticles upon Fe doping, with a 71% degradation of NBB observed. Subsequent co-doping with CeO_2 further enhanced the degradation efficiency by an additional 18% degradation achieved by TF, within a 5.5 h duration. Among the synthesized composites, TFC nanocomposites exhibited the highest photodegradation efficiency, reaching 89% for NBB dye at a concentration of 50 ppm. The kinetics of the photocatalytic degradation process could be well-described by the pseudo-second-order model, with TFC nanocomposites having a reaction rate constant of 9.5×10^{-4} g mg^{-1} min^{-1}. Furthermore, the point of zero charge for the TFC catalyst was determined to be pH 6.4, indicating its favorable surface charge properties. Analysis of the electronic band structure revealed a calculated band gap of 2.60 eV. This study introduces a scalable, co-doped Ce–Fe–TiO_2 nanocomposite with enhanced photocatalytic efficiency, demonstrating a ~25% improvement over TiO_2, a promising direction for advanced dye remediation.

Received 13th April 2025
Accepted 9th July 2025

DOI: 10.1039/d5ra02583d

rsc.li/rsc-advances

Open Access Article. Published on 17 July 2025. Downloaded on 2/10/2026 5:25:23 PM.
This article is licensed under a Creative Commons Attribution-NonCommercial 3.0 Unported Licence.

1. Introduction

In Bangladesh, wastewater generation from textile industries has become a significant problem in recent years, which makes it more difficult to meet the country's UN Sustainable Development Goals.[1–4] Each kilogram of textile goods requires about 100–200 L of water, and a substantial number of synthetic dyes are discharged with wastewater, which is a serious environmental concern.[5] A significant portion of these organic dyes are persistent in the environment and difficult to break down in the natural environmental systems.[6,7]

Naphthol Blue Black (NBB) is such an organic azo dye, extensively used in textile industries which poses a huge alarm due to its structural stability, resistance to biodegradation, blocking sunlight penetration, reducing dissolved oxygen levels, toxicity and carcinogenic potential affecting aquatic life and potentially entering human water supplies.[8–11] Traditional wastewater treatment methods, such as physical and biological,[12,13] are ineffective for synthetic dyes and require a long retention time. Advanced chemical and physical methods like adsorption and coagulation–flocculation are also ineffective and expensive,[12,14] whereas membrane filtration is costly and has fouling and maintenance issues.[15,16]

Advanced oxidation processes (AOPs) have emerged as viable alternatives, leveraging reactive oxygen species (ROS) like hydroxyl radicals (˙OH) to oxidize complex organic pollutants into derivatives.[17,18] Among different AOPs processes, titanium dioxide (TiO_2) based heterogeneous photocatalysis has gained the attention of researchers due to its chemical inertness, low cost, non-toxicity, high oxidation efficiency, reusability, capability to operate in mild conditions and converting organic pollutants into harmless byproducts compared to other processes.[19] For example, oxidation methods (*e.g.*, ozone, Fenton) generate secondary pollutants and require very low pH for

[a]*Department of Chemical Engineering, Bangladesh University of Engineering and Technology, Dhaka-1000, Bangladesh. E-mail: shahinoorislam@buet.ac.bd; Tel: +8801732782120*

[b]*Department of Textile Engineering, Daffodil International University, Dhaka 1341, Bangladesh*

† Electronic supplementary information (ESI) available. See DOI: https://doi.org/10.1039/d5ra02583d

© 2025 The Author(s). Published by the Royal Society of Chemistry

Open Access Article. Published on 17 July 2025. Downloaded on 2/10/2026 5:25:23 PM. This article is licensed under a Creative Commons Attribution-NonCommercial 3.0 Unported Licence.

effective operation.[20,21] However, wide bandgap (~3.2 eV) and rapid recombination of photogenerated electron–hole (e^-/h^+) pairs are the two critical limitations to the practical application of TiO_2-based photocatalysis, which restricts light absorption to the ultraviolet (UV) spectrum only and diminishes quantum efficiency, respectively.[19] To address these challenges and to take advantage of the whole solar energy (UV is ~4% of solar energy), researchers have explored strategies to modify the electronic structure of TiO_2 and enhance photocatalytic performance by doping with transition metals,[2,22,23] rare-earth elements,[24,25] and non-metals.[26,27]

The doping of transition metals, especially iron (Fe), could generate intermediate states, narrowing the bandgap of TiO_2 and extending optical absorption into the visible region.[28] The result is a good use of carriers: the Fe^{3+} ions are suspected to provide electron traps, which might inhibit the recombination of e^-/h^+ thus enhancing charge carrier application.[29–31] For instance, Xia *et al.* reported that calcined Fe-doped TiO_2 nanoparticles achieved a maximum degradation efficiency of 46.3% for methyl orange under visible light, whereas undoped TiO_2 showed significantly lower activity.[32] Other photocatalyst dopants can remarkably promote photocatalytic activity, such as cerium (Ce) with its distinct 4f electron configurations and oxygen reservoir ability. Ce^{4+}/Ce^{3+} redox cycles facilitate electron scavenging, suppress charge recombination, and stabilize reactive oxygen species for achieving a greater degradation performance.[33] For example, Wei *et al.* reported 40% faster degradation rate of rhodamine B with Ce-doped TiO_2 compared to pristine TiO_2.[20] Bhosale *et al.* reported that Ce-doped TiO_2 exhibited superior photocatalytic efficiency for the degradation of a mixture of textile dyes, including rhodamine B, under visible light irradiation.[34] Apart from that, silver (Ag) is well known for its superior ROS production, surface plasmon resonance (SPR), surface adsorption, and electron trapping capabilities and thus, can be useful to degrade synthetic dyes.[35,36] Co-doping of TiO_2 with multiple species might influence the synergistic effects among dopants, which could optimize band structure, surface morphology, charge carrier separation and/or recombination, and light-harvesting efficiency.

While Fe-doped TiO_2 has shown improved photocatalytic activity,[32] a few studies have systematically evaluated the synergistic role of rare-earth elements like Ce in combination with Fe under UV light conditions for the degradation of industrially relevant azo dyes such as Naphthol Blue Black (NBB).[24,34] Developing efficient photocatalysts for dye degradation addresses a critical environmental issue. Since dual-doping like Fe with Ce remains underexplored, this work will fill the gap to develop a novel photocatalyst for degrading a common model azo dye, NBB. Therefore, in this study, a series of doped TiO_2 composites were synthesized, including undoped TiO_2 (T), Fe-doped TiO_2 (TF), Fe–Ce co-doped TiO_2 (TFC), Fe–Ag co-doped TiO_2 (TFA), and Fe–Ce–Ag tri-doped TiO_2 (TFCA) *via* the sol–gel method. The crystalline and morphological properties of the synthesized catalysts were characterized. Additionally, their performance in degrading NBB dye under UV irradiation was investigated to select the best-performing catalyst. The photocatalytic performance of the best-performing catalyst was assessed at different pH, initial dye concentrations, and hydrogen peroxide (H_2O_2) dosages. Finally, a degradation mechanism was proposed by analyzing degradation kinetics using first-order, pseudo-first-order, second-order, and pseudo-second-order equations. The findings from this study could contribute to the design of advanced materials for wastewater treatment applications, offering a sustainable approach to mitigating water pollution.

2. Materials and methodology

2.1 Materials

Titanium(IV) isopropoxide ($Ti(O\text{-}iPr)_4$, 97%), absolute ethanol (CH_3CH_2OH), cerium(III) nitrate hexahydrate ($Ce(NO_3)_3 \cdot 6H_2O$), iron(III) chloride hexahydrate ($FeCl_3 \cdot 6H_2O$, ≥97%), silver nitrate ($AgNO_3$, ≥99%), nitric acid (HNO_3, ≥90%), and naphthol blue black dye (≥80% dye content) were procured from Sigma-Aldrich and used as received. All reagents used were of analytical grade quality.

2.2 Methodology

2.2.1 Catalyst preparation. The catalysts were prepared using the sol–gel method. 50 mL of ethanol was stirred for 15 min. After that, 7 mL of titanium(IV) isopropoxide was added to ethanol, followed by the addition of 30 mL of water to the mixture. Nitric acid solution was added to maintain the pH of the solution at 3 while the mixture was vigorously stirred for 2.5 h to obtain TiO_2 gel.

For monodoping, 3 wt% of iron(III) chloride hexahydrate (with respect to TiO_2) was added after pH adjustment, and the mixture was stirred for an additional 2.5 h to facilitate the gel formation. In the co-doping process, iron(III) chloride hexahydrate was introduced first, followed by 1 h of stirring, after which 3 wt% of either cerium(III) nitrate hexahydrate or silver nitrate was added. Stirring was continued for another 2.5 h to complete gel development.

The resulting gel was aged at ambient conditions for 24 h and subsequently centrifuged (UniCen MR-Herolab) to enhance phase separation. The separated material was dried at 100 °C for 2 h and ground to a fine powder. Calcination was performed in a muffle furnace at 400 °C for 2 h to improve crystallinity. The prepared undoped, doped, and co-doped TiO_2 nanoparticles were stored in a desiccator to minimize atmospheric moisture exposure.

2.2.2 Catalyst characterization. The catalysts were characterized using X-ray diffraction (XRD), Fourier Transform Infrared Spectroscopy (FTIR), Scanning Electron Microscope (SEM) and Energy Dispersive X-ray (EDX). XRD serves as a useful nondestructive technique for nanoparticle characterization, enabling the determination of structure, phase, and crystal size, among other parameters. Using an automated multipurpose X-ray diffractometer, 0.1 g of the catalyst was dehydrated and then exposed to XRD analysis at a wavelength of 0.154 nm. The XRD data was processed using X'pert Highscore Plus Software, and the crystal size was determined by employing the Debye–Scherrer formula[37–39] (eqn (1)).

Open Access Article. Published on 17 July 2025. Downloaded on 2/10/2026 5:25:23 PM. This article is licensed under a Creative Commons Attribution-NonCommercial 3.0 Unported Licence.

$$D = 0.9\lambda/\beta\cos\theta \quad (1)$$

where D = crystal size in nm, λ is the wavelength of light in nm, β is the full width at half maximum in radians and 2θ is the position of the peaks in degrees. FTIR analysis of all the catalysts was performed using a SHIMADZU FTIR-8400, and the obtained images were analyzed manually. SEM images of photocatalysts were obtained for morphological studies using a SEM (Model: Zeiss EVO18, magnification: 500–11 000×, acceleration voltage: 10 kV) and EDX was performed to ensure the metal dopings on TiO_2 are well-proportioned.

2.2.3 Degradation experimentation. Photocatalytic experiments were carried out using 100 mL of dye solutions with varied initial dye concentrations, hydrogen peroxide dosages, pH, and catalyst types. Reactions were conducted within a UV irradiation chamber equipped with four UV-C lamps (25 W each, emission range: 200–280 nm). Five photocatalysts: T, TF, TFC, TFA, and TFCA were evaluated for the photocatalytic degradation of NBB dye under various experimental conditions. The parameters were varied separately, including initial dye concentrations (10, 30, and 50 ppm), pH levels (3, 7, and 11), and H_2O_2 concentrations (0, 0.25, and 0.5 mM). For each experiment, 6 samples of naphthol blue black dye solutions were collected after certain time intervals: 0 min, 30 min, 1.5 h, 2.5 h, 3.5 h, 4.5 h, and 5.5 h. Then, residual dye concentrations were determined using a UV-Vis spectrophotometer. The removal percentage (%) of dye degradations was calculated using eqn (2).

$$\%\ \text{degradation of dye} = \frac{[\text{dye}]_0 - [\text{dye}]}{[\text{dye}]_0} \times 100\% \quad (2)$$

where $[\text{dye}]_0$ and [dye] are the initial and final dye concentrations (ppm).[40]

2.2.4 Kinetics study. The degradation kinetics of NBB dye by T, TF, TFC, TFA, and TFCA photocatalysts were investigated using zero-, first-, second-, pseudo-first-, and pseudo-second-order kinetics models. For the pseudo-first-order and pseudo-second-order kinetics calculation, it was assumed that all NBB degradation occurred *via* adsorption onto the photocatalyst surface. The expressions for these kinetic models are provided as eqn (3)–(9):[41,42]

Zero-order kinetics:

$$C - C_0 = k_0 t \quad (3)$$

First-order kinetics:

$$\ln\left(\frac{C_0}{C}\right) = k_1 t \quad (4)$$

Second-order kinetics

$$\frac{1}{C} - \frac{1}{C_0} = k_2 t \quad (5)$$

Pseudo-first-order kinetics:

$$Q_e = (C_0 - C_e) \times \frac{V}{m} \quad (6)$$

$$Q_t = (C_0 - C) \times \frac{V}{m} \quad (7)$$

$$\ln(Q_e - Q_t) = \ln Q_e - k_3 t \quad (8)$$

Pseudo-second-order kinetics:

$$\frac{t}{Q_t} = \frac{t}{Q_e} + \frac{1}{k_4 \times Q_e^2} \quad (9)$$

The parameters k_0 (ppm min^{-1}), k_1 (min^{-1}), k_2 (ppm^{-1} min^{-1}), k_3 (min^{-1}) and k_4 ($g\ mg^{-1}\ min^{-1}$) represent the apparent kinetic rate constants for zero-order, first-order, second-order, pseudo-first-order, and pseudo-second-order models, respectively. The parameters C_0, C, and C_e represent the initial, time-dependent, and equilibrium dye concentrations (ppm), respectively. Similarly, Q_t and Q_e ($mg\ g^{-1}$) denote the dye adsorbed per unit mass of catalyst at time t and at equilibrium. Here, m (g) corresponds to the mass of catalyst added to a solution volume V (L).

3. Results and discussion

3.1 Characterization of the nanocomposites

3.1.1 FTIR analysis. FTIR analysis was conducted on TiO_2 nanocomposites within the 400–4000 cm^{-1} spectral range. Fig. 1 demonstrates the FTIR spectra, while Table 1 summarizes the findings from the FTIR of photocatalysts. The results confirmed the presence of TiO_2 nanoparticles and the successful incorporation of doping.

The FTIR spectra exhibit a broad absorption band in the range of 3000–3800 cm^{-1}, which is indicative of surface hydroxyl groups and adsorbed moisture.[43] Specifically, in the case of undoped TiO_2 sample (T), the absorption band observed at 3343.48 cm^{-1} corresponds to the stretching of Ti–OH, while the peak at 1633.41 cm^{-1} is associated with the bending vibration of the hydroxyl (O–H) group in water and its interaction with Ti (Ti–OH).[44–46] Similar features were also visible in the other FTIR plots of TF (at 3333.84 cm^{-1} and 1627.14 cm^{-1}), TFC (at 3340.11 and 1648.84 cm^{-1}), TFA (at 3369.03 cm^{-1} and

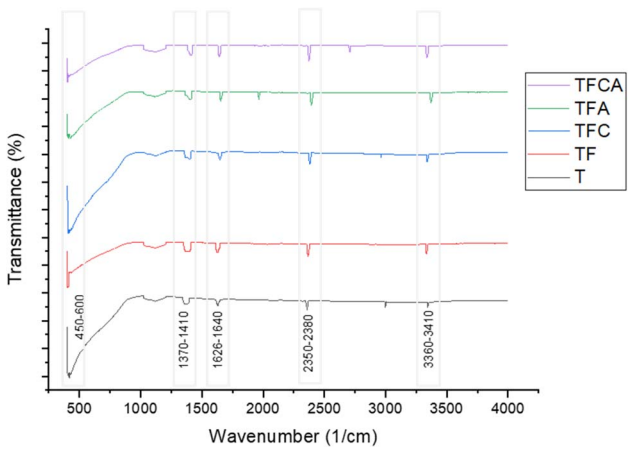

Fig. 1 FTIR spectrum of the photocatalysts.

© 2025 The Author(s). Published by the Royal Society of Chemistry

Open Access Article. Published on 17 July 2025. Downloaded on 2/10/2026 5:25:23 PM. This article is licensed under a Creative Commons Attribution-NonCommercial 3.0 Unported Licence.

Table 1 Summary of FTIR analysis of TiO_2 nanocomposites

Serial no.	Wavenumber (cm^{-1})	Vibrational peak assignment
1	3343.48 (T); 3333.84 (TF); 3340.11 (TFC); 3369.03 (TFA); 3338.18 (TFCA)	Stretching of Ti–OH and O–H bonds
2	2357.55 (T); 2367.68 (TF); 2382.14 (TFC); 2395.64 (TFA); 2374.43 (TFCA)	C═C, C═O bonds
3	1633.41 (T); 1627.14 (TF); 1648.84 (TFC); 1654.14 (TFA); 1644.98 (TFCA)	Bending vibration of Ti–OH and O–H bonds
4	1355.23 (T); 1381.27 (TF); 1399.59 (TFC); 1407.78 (TFA); 1416.46 (TFCA)	Interaction of Ti with hydroxyl in the Ti–O mode
5	418.48 (T); 405.46 (TF); 407.87 (TFC); 411.73 (TFA); 404.01 (TFCA)	Ti–O, Ti–O–Ti bond stretching

1654.14 cm^{-1}), TFCA (at 3338.18 cm^{-1} and 1644.98 cm^{-1}) as summarized in Table 1 and illustrated Fig. 1.

The characteristic Ti–O–Ti and Ti–O stretching vibrations in TiO_2 nanocomposites typically fall within the range of 400–700 cm^{-1}.[47–50] Specifically, the stretching peaks were observed at 418.48 cm^{-1}, 405.46 cm^{-1}, 407.87 cm^{-1}, 411.73 cm^{-1}, and 404.01 cm^{-1} for T, TF, TFC, TFA and TFCA nanoparticles, respectively, confirming the formation of TiO_2-based nanocomposites. Notably, the Ti–O–Ti stretching peaks shift slightly in co-doped samples (*e.g.*, T: 418.48 cm^{-1} → TFC: 407.87 cm^{-1}), indicating lattice modifications due to dopant-induced bond length changes. Absence of Fe–O (typically 450–600 cm^{-1}) or Ce–O (500–750 cm^{-1}) vibrational modes might be attributed to low dopant concentrations or overlapping with TiO_2 peaks. Nevertheless, it's essential to note that FTIR analysis may lack sensitivity towards low doping levels and can be hindered by weak infrared absorption and the potential overlap of trace material peaks by significant components.[2,51] Additional peaks near 2360 cm^{-1} are attributed to C═C and C═O bonds originating from the titanium isopropoxide precursor and other organic solvents used in synthesis.[52] Furthermore, peaks near 1400 cm^{-1} are associated with the interaction of Ti–O with the O–H group.[44] However, in contrast to other nanocomposites, this peak is less noticeable in TiO_2.

3.1.2 XRD analysis. XRD analysis was conducted on all synthesized T, TF, TFC, TFA, and TFCA samples. The resulting phase condition graphs are depicted in Fig. 2. In the case of pure TiO_2, the XRD graph displayed a prominent peak at 2θ of 25.26° corresponding to the 101 planes, indicative of the presence of anatase TiO_2, as reported in previous studies.[53–55] Both undoped and doped TiO_2 nanoparticles displayed characteristic diffraction peaks primarily attributed to the anatase nanocrystal phase. These peaks were observed at 2θ angles of 25.48° (101), 37.80° (004), 48.15° (200), 55.19° (211), 62.79° (204), 70.47° (220), and 75.16° (215), respectively. The preference for the anatase phase is notable for its efficacy in dye degradation and the modification of tetragonal crystal structures.[56] XRD patterns for the graphs of other photocatalysts exhibited a similar trend to pure TiO_2, suggesting that the incorporation of Fe_2O_3, CeO_2, and Ag_2O did not alter the arrangement of the crystal lattice, as confirmed by previous research.[56–58] The absence of distinctive peaks of Fe_2O_3, CeO_2 and Ag_2O in the graphs suggests either substitutional incorporation of the dopants into the TiO_2 lattice and/or a homogeneously dispersed distribution of dopants at a minute level. Hence, it is evident that adding Fe_2O_3, CeO_2, and Ag_2O did not significantly alter the anatase structure, as they are highly dispersed in the structure of TiO_2.[59] The anatase TiO_2 peak intensity and peak location somewhat shifted with the addition of iron, cerium, and silver, suggesting the development of more stable crystals.[60]

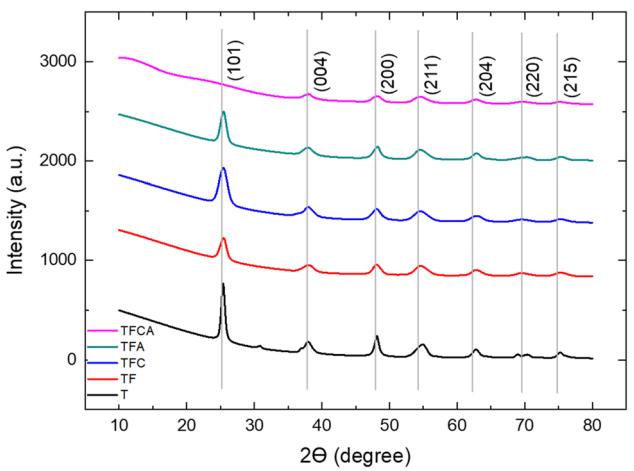

Fig. 2 XRD plot of the prepared nanoparticles.

The average crystal size was determined using the Debye–Scherrer formula, as described by eqn (1).[61–63] For pure TiO_2, the crystal size was measured at 13.32 nm, while the TF, TFC, TFA, and TFCA catalysts containing anatase exhibited average crystal sizes of 7.56 nm, 5.92 nm, 8.38 nm, and 5.15 nm, respectively (Table 2). Co-doped catalysts (TFC: 5.92 nm, TFCA: 5.15 nm) exhibit smaller crystallite sizes compared to undoped TiO_2 (13.32 nm), indicating lattice strain from dopant integration.[64] Crystallographic lattice constants were calculated using eqn (10), where a and c are lattice parameters, h, k, l denote Miller indices, and d is the interplanar spacing. For pristine TiO_2, the lattice parameters were found to be $a = 3.7765$ Å and $c = 9.5116$ Å, whereas for the TFC nanocomposite, values of $a = 3.7732$ Å and $c = 9.5373$ Å were observed. These minimal shifts suggest successful substitutional doping without significant lattice distortion, thereby maintaining the structural framework.[65] It has been suggested that smaller crystalline sizes could positively impact photocatalytic performance.[66] The relative anatase and rutile content was estimated using eqn (11), where W_R denotes the rutile mass fraction, and I_R and I_A correspond to the intensities of the [211] and [101] diffraction peaks, respectively. Co-doped nanocomposites showed negligible alterations in phase composition, indicating that both anatase and rutile phases remained suitable for catalytic activity.[67–69] Fe and Ce doped TiO_2-based nanomaterials are well known for their

Open Access Article. Published on 17 July 2025. Downloaded on 2/10/2026 5:25:23 PM. This article is licensed under a Creative Commons Attribution-NonCommercial 3.0 Unported Licence.

Table 2 Physicochemical properties of the prepared photocatalysts

Sample	Method	Crystalline size (nm)	Anatase phase (%)	Rutile phase (%)	Lattice spacing, d_{hkl} (Å)	Lattice parameters (Å)		Volume of unit cell, V (Å^3)
						a	c	
T	Sol–gel	13.32	78.75	21.25	3.5062	3.7765	9.5116	135.6540
TF	Sol–gel	7.56	66.07	33.93	3.4916	3.7744	9.4557	134.7068
TFC	Sol–gel	5.92	70.62	29.38	3.4991	3.7732	9.5373	135.7829
TFA	Sol–gel	8.38	70.03	29.97	3.4982	3.7693	9.4977	134.9397
TFCA	Sol–gel	5.15	58.64	41.36	2.3642	3.7817	9.4783	135.5516

structural stability even after being used several times.[70,71] Although the post-degradation XRD analysis of the TFC sample was not included in this study, based on prior studies involving similar Ce and Fe-doped TiO_2 systems, the structural integrity of the photocatalyst is expected to remain stable after the photocatalytic degradation process.

$$\frac{1}{d^2} = \frac{4(h^2 + hk + k^2)}{3a^2} + \frac{l^2}{c^2} \quad (10)$$

$$W_R = \frac{1}{1 + 1.265\ \frac{I_R}{I_A}} \quad (11)$$

3.1.3 SEM analysis. Surface morphology analysis of nanoparticles T, TF, TFC, TFA, and TFCA was conducted using SEM imaging, as detailed in Fig. 3. The SEM images were captured at a magnification of 30 000×, revealing that all nanoparticles were in the range of 10–140 nm. Additionally, dense agglomeration of the nanoparticles was observed across the images. The nanoparticles exhibited irregular shapes, contributing to the roughness of the nano-catalyst surfaces. This irregular morphology and agglomeration are well-documented characteristics of TiO_2 nanoparticles, confirmed by similar research studies.[72–75]

The microscale SEM images of the nanoparticles provide a detailed understanding of the doping effects and enable comparison among different nanocomposites. In Fig. 3, images magnified by 10 000× depict T (Fig. 3a), TF (Fig. 3b), TFC (Fig. 3c), TFA (Fig. 3d), and TFCA (Fig. 3e), revealing that doping significantly influences the size of agglomerated particles, with cerium doping resulting in the smallest aggregated particle size. These microscale images also indicate that the surface roughness of the doped nano-photocatalysts surpasses that of undoped TiO_2.[72,76,77] Furthermore, modifying TiO_2 with metals such as Fe, Ce, and Ag increases surface roughness and rigidity, leading to a more porous surface area. In Fig. 3f, the box and whisker plot illustrates that the first and second quartiles of the catalysts are predominantly below the 100 nm range. The mean diameters, measured using ImageJ software from SEM images, range from 80 to 130 nm for T, TF, TFC, TFA, and TFCA nanocatalysts.[78,79]

The incorporation of Fe, Ce and Ag dopants into TiO_2 was further supported by EDX mapping. Based on the data presented in Table S1† from the EDX mapping analysis, it was observed that the prepared doping ratio exhibits minimal deviation from the ratio determined through EDX mapping. This consistency confirmed the reliability of the TFCA catalyst preparation process. Furthermore, Fe, Ce, Ag, and O elements were uniformly dispersed across the entire TFCA catalyst, as illustrated in Fig. S1.† Although agglomeration was observed in microscale SEM images, the elemental proportions remained evenly distributed.

3.1.4 Band gap energy and band edge position. In order to investigate electronic transitions and estimate band gap energy (E_g), measurements of UV-visible diffuse reflectance spectra utilizing absorption edge wavelengths were examined. The Kubelka–Munk and Tauc equations (eqn (12) and (13)) are the most widely used and accurate technique for calculating E_g.[80,81]

$$K = \frac{(1 - R)^2}{2R} \quad (12)$$

$$(\alpha h\nu) = \beta(h\nu - E_g)^n \quad (13)$$

Here, R (%) signifies the absolute reflectance, and K is its Kubelka–Munk transformed value. Planck's constant (6.626×10^{-34} J s) and light frequency (ν) were incorporated to compute absorption properties. The absorption coefficient (α) was calculated *via* the Beer–Lambert law, while β represents a material-specific absorption constant. The exponent n is associated with the nature of electronic transitions within the semiconductor: taking values of 1/2, 3/2, 2, and 3 for direct allowed, direct forbidden, indirect allowed, and indirect forbidden transitions, respectively. Fig. S2† displays Tauc plots generated from reflectance data using the Kubelka–Munk and Tauc equations. By extrapolating the linear regions of these plots to the photon energy axis, the bandgap energies (E_g) of the catalysts were estimated. The E_g values for T, TF, TFC, TFA, and TFCA were found to be 2.9, 2.8, 2.6, 2.65, and 2.35 eV, respectively (Fig. S2†), highlighting the bandgap narrowing effect induced by co-doping. Co-doped samples (TFC: 2.6 eV, TFCA: 2.35 eV) show narrow bandgaps compared to undoped TiO_2 (2.9 eV), consistent with successful electronic structure modification *via* co-doping. A comparable percentage of the rutile phase in the TiO_2 structure may also contribute to the reduction of the band gap in addition to doping, as shown in Table 3.

The Mulliken electronegativity theory offers a method to estimate the conduction band (CB) and valence band (VB)

 © 2025 The Author(s). Published by the Royal Society of Chemistry

Open Access Article. Published on 17 July 2025. Downloaded on 2/10/2026 5:25:23 PM.
This article is licensed under a Creative Commons Attribution-NonCommercial 3.0 Unported Licence.

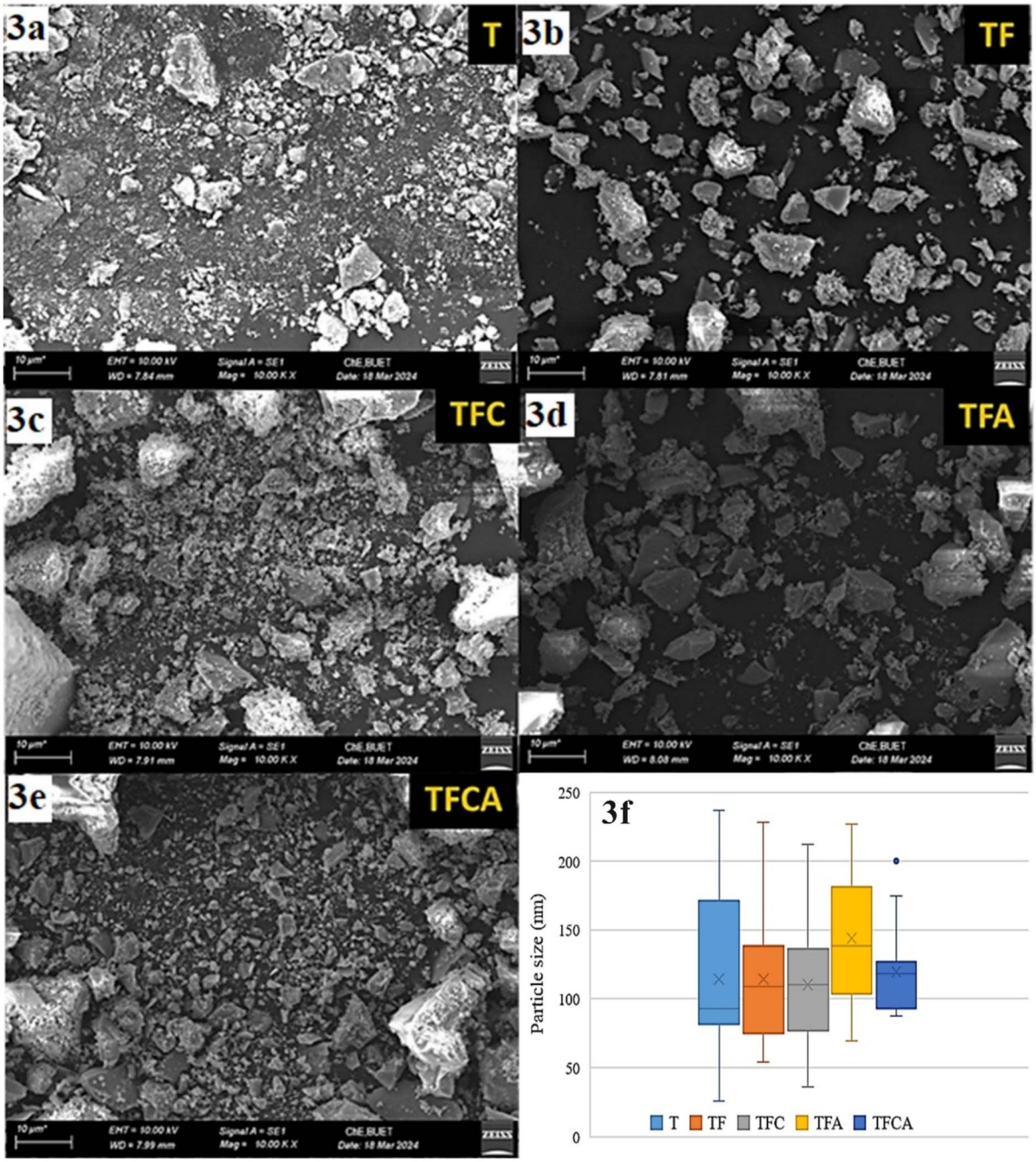

Fig. 3 Microscale SEM images of different nano-photocatalysts; (a) undoped TiO_2, (b) TiO_2 doped with Fe (TF), (c) co-doped with Fe_2O_3–CeO_2 (TFC), (d) Fe_2O_3–Ag_2O (TFA), (e) Fe_2O_3–CeO_2–Ag_2O (TFCA) and (f) particle size analysis of different nanophotocatalysts.

Table 3 CB and VB potentials of prepared photocatalysts

Catalyst	$X_{catalyst}$	E_g (eV)	E_{VB} (eV)	E_{CB} (eV)
T	5.804773	2.90	2.75	−0.15
TF	5.841403	2.80	2.74	−0.06
TFC	5.763471	2.60	2.56	−0.04
TFA	5.687085	2.65	2.51	−0.14
TFCA	5.659762	2.35	2.33	−0.02

potentials of a semiconductor.[82–85] The used equations are stated in eqn (14)–(16).

$$E_{VB} = \chi - E_e + 0.5E_g \quad (14)$$

$$\chi_{catalyst} = [\chi_A{}^a \chi_B{}^b \chi_C{}^c]^{1/(a+b+c)} \quad (15)$$

$$E_{CB} = E_{VB} - E_g \quad (16)$$

Open Access Article. Published on 17 July 2025. Downloaded on 2/10/2026 5:25:23 PM. This article is licensed under a Creative Commons Attribution-NonCommercial 3.0 Unported Licence.

Here, E_{VB}, E_{CB}, E_e, and χ represent the valence band potential, conduction band potential, standard hydrogen electrode potential (~4.5 eV), and absolute electronegativity of the semiconductor catalysts, respectively. χ_A, χ_B, χ_C denote the geometric mean of the electronegativities of atoms A, B, and C, constituting the catalyst, while a, b, and c represent the numbers of atoms in the catalyst formula unit. All necessary information for calculating χ, CB, and VB potentials is provided in Tables S2† and 3, while the band position of the catalyst is presented in Fig. S3.†[85–87]

In several instances, the low concentration of dopants made it challenging to observe distinct and well-resolved dopant peaks. Although XPS analysis was not performed in this study due to the unavailability of necessary instrumentation, the incorporation of dopants and corresponding structural modifications were validated using FTIR, XRD, SEM-EDX, and UV-vis DRS. These complementary techniques collectively confirm the effective substitutional doping and enhanced photocatalytic potential. The absence of XPS and BET analyses is acknowledged as a limitation of this work. Future investigations will incorporate XPS-based depth profiling and surface hydroxyl quantification to provide further insight into the dopant oxidation states and mechanistic pathways. Additionally, although BET surface area and pore size analyses could not be conducted due to time and equipment constraints, indirect indicators, such as crystallite size reduction, improved dye adsorption capacity, and rough SEM-observed morphology, strongly suggest the presence of favorable surface characteristics in the doped photocatalysts. These observations will be further supported in future work through detailed BET and BJH analyses to strengthen the understanding of structure–activity relationships.

3.2 Dye degradation analysis

3.2.1 Effect of different photocatalysts. The impact of different catalysts on the degradation of NBB dye is shown in Fig. 4. The concentration degradation results have shown that the TFC catalyst facilitates the maximum 89.13% degradation of the dye. The other catalysts T, TF, TFA, and TFCA assisted in 63.84%, 71.32%, 74.69% and 81.21% degradation, respectively, in the selected 50 ppm dye, pH 3 and 0.25 mM H_2O_2 condition. It is evident from the removal trend shown in Fig. 4 that every catalyst displayed a significant initial rate of degradation. After around 210 min, the degradation rate slowed a plateaued for all catalysts, with the exception of TFC, which required about 260 min. The degradation curve was the steepest in the first 30 min, indicating that the degradation rate in the first 30 min was the highest.

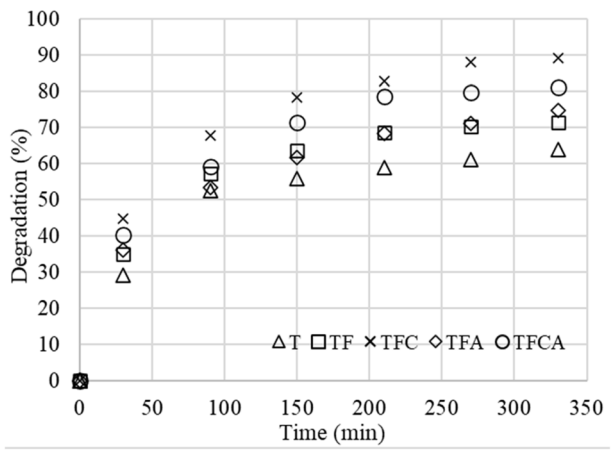

Fig. 4 Effect of photocatalyst (catalyst amount: 0.10 g, pH: 3.0, 0.25 mM H_2O_2, dye: 50 ppm and UV light exposure: 330 min).

As mentioned above, the rough surface area and low band gap energy (2.6 eV) may have contributed to the impact of the addition of CeO_2. It is anticipated that a tiny amount of energy will be used to generate charge carriers due to the narrow band gap. Furthermore, given the intended surface interactions, a rough surface area indicates a more active absorbent. Additionally, the deposition of Ag on TFC showed fewer improvements in photocatalytic activity than TFC, while the band gap of TFCA was the lowest (2.35 eV). The probable reason for this might be the increasing tendency to charge recombination and thus, fewer available electrons and holes to react with the dye molecule.[88] The sequence of photocatalytic degradation rates observed was TFC > TFCA > TFA > TF > T. The experimental findings indicate that incorporating Fe and Ce nanoparticles onto the TiO_2 catalyst surface can enhance the photodegradation efficiency. Now, the effect of pH, initial dye concentration, and time was evaluated for the best catalyst *i.e.* TFC in the following section.

3.2.2 Point of zero charge (PZC) and effect of pH. In a photocatalytic setup using a TiO_2-based photocatalyst, the pH at which the net charge of the particles equals zero is known as the isoelectric point or PZC. This parameter is crucial in understanding the variable-charge surfaces of photocatalysts during photocatalysis. Literature suggests that the isoelectric point of TiO_2 particles falls within the pH range of 6 to 7.5.[89] Generally, when the solution pH exceeds the PZC, TiO_2 particles tend to adsorb positively charged pollutants, whereas when the pH is below the PZC, they tend to attract negatively charged contaminants. Consequently, controlling the pH of the photocatalytic system can modify the surface charge of the photocatalysts, offering the potential for selectively degrading charged pollutants.[90] For instance, Duffy *et al.* highlighted the significance of solution pH in selectively degrading a pollutant mixture of acetic acid and 2-chlorobiphenyl.[91] By adjusting the pH from neutral to basic, they were able to selectively degrade 2-chlorobiphenyl in the presence of higher levels of acetic acid, as the solution's pH influenced the photodegradation rate of acetic acid. In a similar manner, regulating the pH allowed for the targeted photodegradation of 4-hydroxybenzoic acid or benzamide. At pH 4, TiO_2 photocatalysts favored decomposing negatively charged 4-hydroxybenzoic acid, while at pH 8, they were inclined towards degrading positively charged benzamide.[92]

In the experiment, the TFC catalyst was used to identify the PZC of the catalyst. PZC values for TFC were determined in 1 M NaCl or $NaNO_3$ solution at 303–333 K. In this method, the sample (0.2 g) and 1 M NaCl or $NaNO_3$ (40 mL) were mixed in

 © 2025 The Author(s). Published by the Royal Society of Chemistry

Open Access Article. Published on 17 July 2025. Downloaded on 2/10/2026 5:25:23 PM. This article is licensed under a Creative Commons Attribution-NonCommercial 3.0 Unported Licence.

different reaction breakers. The initial pH of the suspensions was systematically adjusted to values of 2, 4, 6, 8, and 10 using dilute solutions of nitric acid (HNO_3) or sodium hydroxide (NaOH), with continuous monitoring *via* a calibrated pH meter. Each suspension was subsequently placed in a shaker water bath and agitated for 24 h to ensure equilibrium. Following this period, the suspensions were allowed to settle, and the final pH values were carefully recorded. The pH shift (ΔpH), defined as the difference between the final and initial pH, was calculated for each sample and plotted against the corresponding initial pH values (Fig. S4†). The point at which ΔpH equals zero was identified as the PZC.[93] The value of PZC found in Fig. S4† is 6.4.

According to theory, NBB dye, being an acidic dye, should degrade more effectively when the pH of the reaction medium is maintained below 6.4.[2,94] However, to find the optimum pH, 10 ppm NBB dye degradation experiments were conducted at pH levels of 3, 7, and 11 to verify this. Fig. 5 illustrates the degradation outcomes of NBB dye in the presence of TFC catalyst. The results indicated that at pH 3, the degradation of NBB dye increased by more than 18% and 28% compared to that achieved at pH 7 and pH 11, respectively. This finding confirms that at pH 3, NBB dye degrades more efficiently compared to neutral or basic pH conditions, supporting the isoelectric phenomenon.[95,96]

3.2.3 Effect of initial dye concentration. The degradation performance of the dye was notably affected by its initial concentration. When using TFC, approximately 80% degradation of 10 ppm NBB dye was observed after 330 min of UV light exposure. Consequently, during photocatalysis, the initial dye concentration was raised to 30 and 50 ppm while keeping all other operating parameters constant, as shown in Fig. 6. For the TFC nanocatalyst, the photodegradation efficiency of 30 ppm NBB dye was 76% after 330 min of UV light exposure.

Conversely, maintaining all parameters constant, the minimum dye degradation (66.12%) was observed at a concentration of 50 ppm dye. The experimental data reveal that higher initial NBB dye concentrations diminish photocatalytic efficiency due to two interrelated mechanisms. First, excess dye molecules occupy a greater proportion of the catalyst's active sites, limiting the availability of surface regions for hydroxyl ion adsorption and suppressing the production of reactive oxidizing species such as hydroxyl radicals (˙OH). Second, elevated dye concentrations attenuate UV light penetration through the solution, promoting competitive adsorption of dye molecules on the catalyst surface. This dual effect—reduced radical generation and light shielding—significantly hinders degradation kinetics at higher pollutant loads.[60,97] Strategies such as prolonging UV light exposure time, increasing intensity, and adding external oxidants (H_2O_2) should be employed in the photocatalytic process to overcome these challenges. To optimize the hydrogen peroxide, 50 ppm dye was used to compare the different degradation results better.

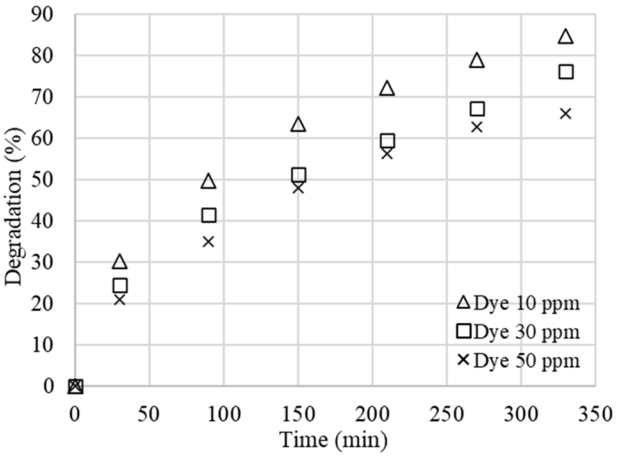

Fig. 6 Effect of initial dye concentration (catalyst: TFC, dose: 0.10 g, pH: 3.0, 0.1 mM H_2O_2 and UV light exposure: 330 min).

3.2.4 Blank experiments. In order to understand the parameters' sole effect on degrading NBB dye, five blank experiments were performed. Details of the reaction conditions are shown in Table S3† and the results are shown Fig. 7. In the initial experiment, the focus was solely on assessing the impact

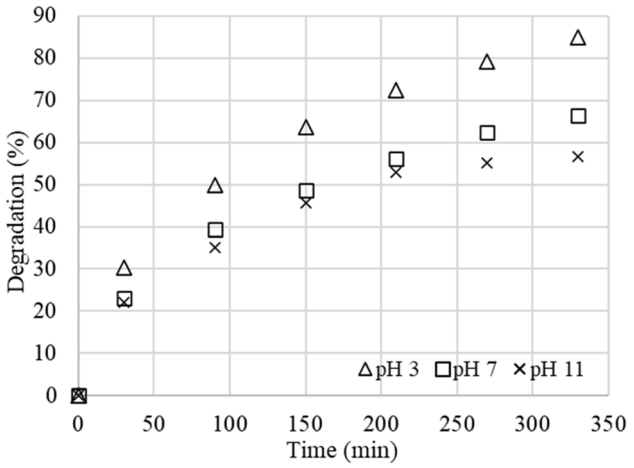

Fig. 5 Effect of pH on NBB degradation (catalyst: TFC, dose: 0.10 g, dye: 10 ppm, 0.1 mM H_2O_2 and UV light illumination: 330 min).

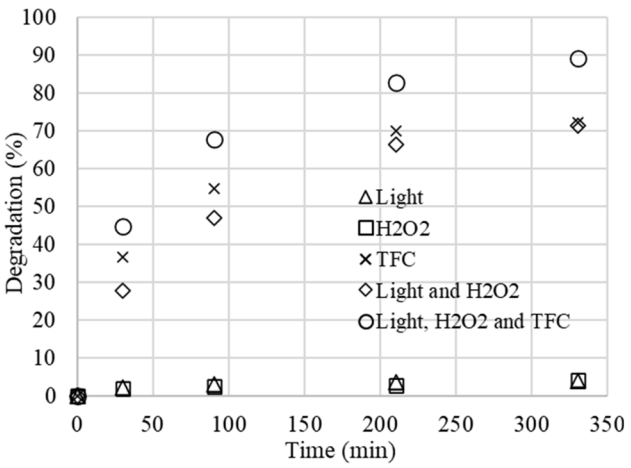

Fig. 7 Individual and combined effect of degradation parameters in NBB dye degradation.

Open Access Article. Published on 17 July 2025. Downloaded on 2/10/2026 5:25:23 PM. This article is licensed under a Creative Commons Attribution-NonCommercial 3.0 Unported Licence.

of light exposure (photolysis) on the degradation of a 50 ppm NBB dye solution. Under these conditions, without the use of a catalyst or H_2O_2, a lower degradation rate of 3.93% was observed over a 330 min reaction period, maintaining a pH of 3. Subsequently, the influence of H_2O_2 was examined under similar conditions to previous experiments without light exposure. The introduction of 0.25 mM H_2O_2 led to a slightly increased degradation rate of 4.21%, indicating a marginal enhancement in the absence of light. In the next experiment, the sole impact of the catalyst was investigated by employing a TFC catalyst without adding H_2O_2 or exposure to light. Remarkably, a substantial degradation rate exceeding 71% was achieved under these conditions, suggesting the catalytic activity of TFC in the absence of additional oxidants or light. Next experiment was performed to find the combined effects of H_2O_2 and light without a catalyst. Notably, a degradation rate of over 71% was attained, indicating the synergistic impact of these factors on the degradation process. Finally, all parameters, including the TFC catalyst, H_2O_2, and light exposure, were used, and the degradation efficiency was found to exceed 89%. Including the TFC catalyst in the final experiment led to a substantial enhancement, yielding an additional 18% degradation compared to the scenario without the catalyst. These findings emphasize the TFC catalyst's significant role in catalyzing the degradation of the NBB dye, particularly when combined with other reactive agents such as H_2O_2 and light and achieving notable improvements in degradation efficiency.

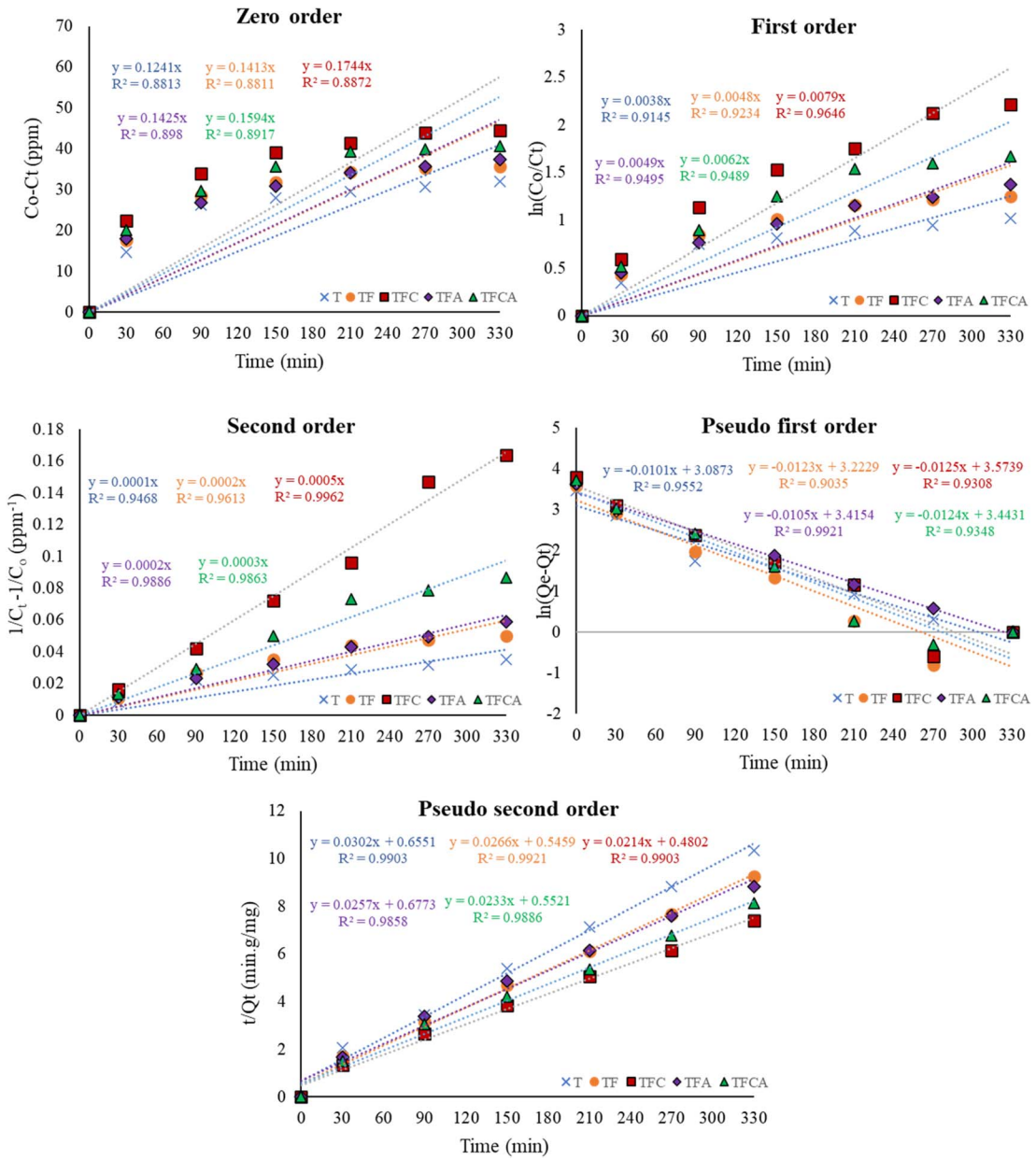

Fig. 8 NBB dye degradation kinetics plotted against various photocatalysts (dye: 50 ppm, UV light illumination: 330 min, pH: 3.0, 0.25 mM H_2O_2, catalyst dose: 0.10 g).

© 2025 The Author(s). Published by the Royal Society of Chemistry

Open Access Article. Published on 17 July 2025. Downloaded on 2/10/2026 5:25:23 PM. This article is licensed under a Creative Commons Attribution-NonCommercial 3.0 Unported Licence.

3.3 Kinetics analysis

In order to advance wastewater treatment technologies for textile and industrial effluents, the determination of degradation kinetics is a pivotal aspect. Such a discovery is essential for efficiently constructing, improving, and scaling up photocatalytic reactors. In this study, the photocatalytic degradation kinetics of the NBB dye degradation were evaluated through the use of various kinetic models, including zero order, first order, second order, pseudo-first-order, and pseudo-second-order models, with respect to dye concentration.[2] The kinetic plots for all catalysts are visually represented in Fig. 8, while the comprehensive results of regression coefficients (R^2), rate constants (k), and the quantity of dye absorbed (for pseudo-first and second-order) are presented in Table 4.

R^2 value served as an important tool for identifying the most fitting model for evaluating degradation kinetics. Upon comparison, it was found that the photocatalytic degradation kinetics consistently aligned with the pseudo-second-order model across all catalysts, under conditions of 50 ppm dye concentration and 0.25 mM H_2O_2 concentration. Moreover, the pseudo-second-order model exhibited an impressive fit ranging between 98% to 99% for the T, TF, TFC, TFA, and TFCA photocatalysts. Additionally, upon evaluating the quantity of dye absorbed (Q_e) among the catalysts, it was evident that TFC exhibited the highest values, indicative of its superior adsorption capacity relative to other catalysts. The pseudo-second-order rate constants ($k_4 \sim$ g mg^{-1} min^{-1}) ranged between 9.54 to 13.9 $\times$ 10^{-4} g mg^{-1} min^{-1}.

Furthermore, the second-order model was also found to be better fitted with degradation data, with R^2 values ranging between 94% and 99%. These results signify that higher concentrations of the reactant (dye) correspond to enhanced degradation rates. Besides this model, only the pseudo-first-order and first-order models exhibited significant fitting, while the zero-order model failed to represent the experimental data. Finally, it was evident from the data that a pronounced tendency towards pseudo-second-order behavior was observed. This observation suggested a prevailing mechanism which is not only diffusion-controlled but also governed by adsorption-controlled surface-active sites where pollutant molecules interact with photocatalytically generated reactive species (*e.g.*, $^{\bullet}$OH, $O_2^{\bullet-}$).[98,99]

3.4 Proposed degradation mechanism

Based on the band energy levels relative to the Normal Hydrogen Electrode (NHE) and the degradation outcomes, it was observed that the TFC catalyst exhibited more significant UV light activity compared to other photocatalysts. Consequently, a degradation mechanism based on the band energy levels of TFC is proposed for NBB dye degradation. When exposed to UV light, electrons generated by TFC's valence band undergo a faster transfer process than electron–hole recombination within TFC. Conversely, TFCA, with its narrower band gap, was expected to facilitate degradation more efficiently, but the probability of electron–hole recombination prevails. TFC generates more electron–hole pairs under UV light, transferring them between semiconductors. Specifically, electrons in the CB of TFC produce $O_2^{\bullet-}$, which aids dye degradation. CeO_2 may possess a more positive redox potential than TiO_2, and therefore, electrons from TiO_2's CB readily transfer to CeO_2's CB and then Fe_2O_3's CB. Conversely, TiO_2's VB may transfer created holes to CeO_2's VB, enhancing hydroxyl radical synthesis and minimizing charge recombination. Fe_2O_3's VB holes also do the same (Fig. 9).[72,100–102]

Although the identification of intermediate compounds would have strengthened the validation of the proposed mechanism, the interpretation presented in this study was supported by literature reports of similar photocatalytic systems.[18,103] Previous studies have established the bandgap energies of TiO_2, Fe_2O_3, and CeO_2 at 3.2 eV, 2.1 eV, and 2.9 eV, respectively.[94,104,105] The oxidative potential of photogenerated holes in these materials facilitates water dissociation, producing hydroxyl radicals ($^{\bullet}$OH) that oxidize adsorbed NBB molecules. Simultaneously, conduction band electrons reduce dissolved oxygen to yield superoxide radicals ($O_2^{\bullet-}$) and additional $^{\bullet}$OH species.[2,106] These reactive intermediates drive the sequential cleavage of NBB's azo bonds and aromatic rings (reactions (4.9)–(4.17)), ultimately mineralizing the dye into CO_2 and H_2O. Although total organic carbon (TOC) analysis was not performed in this study, the pseudo-second-order kinetics, high

Table 4 Kinetic parameters of NBB dye degradation by different photocatalysts

Catalyst			T	TF	TFC	TFA	TFCA
Kinetic parameters	Zero order	k_0 (ppm min^{-1})	0.12	0.14	0.17	0.14	0.16
		R^2	0.88	0.88	0.89	0.9	0.89
	First order	$k_1 \times 10^{-3}$ (min^{-1})	3.8	4.8	7.9	4.9	6.2
		R^2	0.91	0.92	0.96	0.95	0.95
	Second order	$k_2 \times 10^{-3}$ (ppm^{-1} min^{-1})	0.1	0.2	0.5	0.2	0.3
		R^2	0.95	0.96	0.99	0.99	0.99
	Pseudo first order	$k_3 \times 10^{-3}$ (min^{-1})	1.39	1.29	0.95	0.98	0.98
		Q_e (mg g^{-1}) calc.	33.11	37.59	46.73	38.91	42.92
		Q_e (mg g^{-1}) exp.	31.92	35.66	44.56	37.35	40.60
		R^2	0.96	0.90	0.93	0.99	0.93
	Pseudo second order	$k_4 \times 10^{-4}$ (g mg^{-1} min^{-1})	13.92	12.96	9.54	9.75	9.83
		Q_e (mg g^{-1})	33.11	37.59	46.73	38.91	42.92
		R^2	0.99	0.99	0.99	0.99	0.99

Open Access Article. Published on 17 July 2025. Downloaded on 2/10/2026 5:25:23 PM.
This article is licensed under a Creative Commons Attribution-NonCommercial 3.0 Unported Licence.

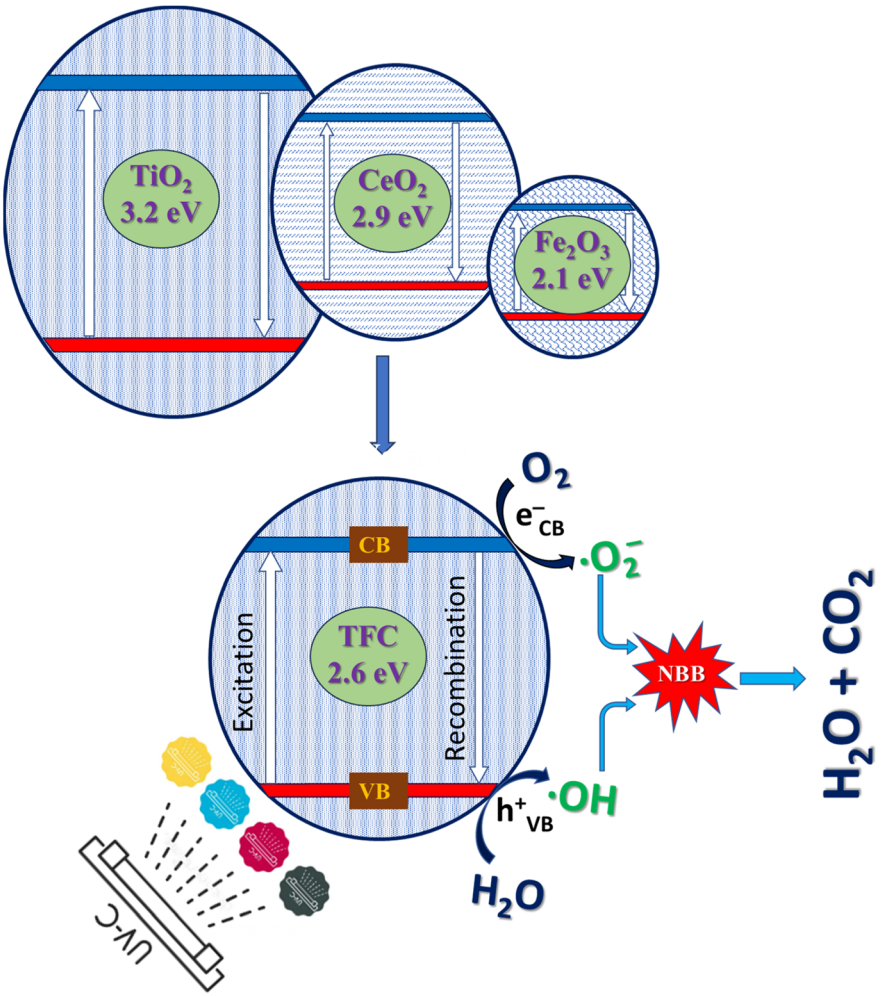

Fig. 9 Proposed degradation mechanism of NBB dye using TFC catalyst in the presence of UV irradiation.

degradation efficiency (up to 89%), and proposed radical-mediated mechanism collectively indicate the potential for high mineralization. Future studies will incorporate TOC and Inorganic Carbon (IC) analyses to confirm complete oxidation of the dye molecules.

Moreover, peroxyl radicals have the potential to react with protons and superoxide anions, resulting in the production of H_2O_2 and oxygen molecules. Once H_2O_2 is generated, exposure to UV radiation can prompt its decomposition into $^{\bullet}OH$. Additionally, molecular oxygen can act as an electron acceptor scavenger, forming $O_2^{\bullet-}$ and hydrogen peroxide. Consequently, the adsorbed NBB dye molecules on the catalyst surface undergo reactions with $^{\bullet}OH$ and $O_2^{\bullet-}$ to yield simple products such as water and CO_2 (Fig. 9).[53,107,108]

Compared to others, this photocatalytic process renders the TFC photocatalyst highly active under UV light exposure. Consequently, the heterostructure of TFC effectively restrains the recombination of h^+/e^-pairs, further enhancing its catalytic efficiency.

$$TFC + h\nu \rightarrow h_{VB}^{+} + e_{CB}^{-} \quad (17)$$

$$H_2O_{ad} + h^+ \rightarrow {}^{\bullet}OH + H^+ \quad (18)$$

$$NBB_{ad} + e_{CB}^{-} \rightarrow NBB^{-} \quad (19)$$

$$OH_{ad}^{-} + h^+ \rightarrow {}^{\bullet}OH \quad (20)$$

$$O_2\ (\text{adsorbed}) + e_{CB}^{-} \rightarrow O_2^{\bullet-} \quad (21)$$

$$O_2^{\bullet-} + H^+ \rightarrow HO_2^{\bullet} \quad (22)$$

$$O_2^{\bullet-} + H^+ + HO_2^{\bullet} \rightarrow H_2O_2 + O_2 \quad (23)$$

$$H_2O_2 + h\nu \rightarrow 2{}^{\bullet}OH \quad (24)$$

$$^{\bullet}OH/O_2^{\bullet-}/HO_2^{\bullet} + NBB \rightarrow \text{intermediates} \rightarrow CO_2 + H_2O \quad (25)$$

3.5 Comparison with other photocatalysts

A comparative analysis was conducted to evaluate the photocatalytic efficacy of the as-synthesized TFC in relation to various photocatalysts documented in the literature. Parameters such as light source, degradation percentage, type of photocatalyst,

© 2025 The Author(s). Published by the Royal Society of Chemistry

Open Access Article. Published on 17 July 2025. Downloaded on 2/10/2026 5:25:23 PM. This article is licensed under a Creative Commons Attribution-NonCommercial 3.0 Unported Licence.

Table 5 Comparison of degradation performance of TFC photocatalyst with other photocatalysts reported in the literature

Photocatalyst	Parameters and process conditions	Removal efficiency	Reference
Fe–TiO_2	*Para*-nitrophenol degradation; prepared hydrothermally with ultrasonic assistance; visible light 5 h	92%	109
N–Fe–Cu–TiO_2 nanoparticles	Methylene blue degradation; sol–gel; 2 h sunlight exposure	95.5%	110
Er^{3+}:$YAlO_3$/Fe–Co–TiO_2–ZnO	Azo fuchsine degradation; sol–gel; visible light 2 h	47.8%	111
N–TiO_2/SiO_2/Fe_3O_4 nanoparticles	Phenol degradation; visible light for 270 min; hydrolysis, condensation, dispersion, and calcination	64%	112
$Co_{0.5}Zn_{0.25}M_{0.25}Fe_2O_4$–$TiO_2$	Methyl orange degradation; co-precipitation, hydrolysis and thermal treatment; visible light 5 h	80%	113
$Co_{0.5}Zn_{0.25}M_{0.25}Fe_2O_4$–$TiO_2$	Methylene blue degradation; co-precipitation, hydrolysis and thermal treatment; visible light 5 h	75%	113
Fe_3O_4/TiO_2–S with surface hydroxyls	Rhodamine B degradation; one pot with hydrothermal and reverse precipitation; 60 min of solar light	100%	114
Fe_3O_4/TiO_2–S with surface hydroxyls	Formaldehyde degradation; one pot reverse precipitation and hydrothermal; 60 min of simulated solar light	100%	114
$AgFeO_2$/CNTs/TiO_2	Methyl orange degradation; 5 kV, 1 L min^{-1} air supply, 2 min for treatment	95%	115
Fe_2O_3–TiO_2 with $Na_2S_2O_8$	Dimethyl phthalate degradation; 14 kV, pH: 3, air supply (0.5 L min^{-1}), argon supply (4.5 L min^{-1})	100%	116
Fe-doped TiO_2/rGO nanocomposite	Rhodamine B degradation; solar; 0.6 g per L nanocomposite; pH: 6.0; time: 120 min	91%	117
TiO_2-modified Fe_3O_4 nanocomposite	Rhodamine-6G (Rh6G) in textile wastewater degradation; chemical co-precipitation method; visible light 60 min; 150 W light	100%	118
TiO_2/montmorillonite/Fe_3O_4	Methylene blue degradation; UV light 80 min; 100 W light	94%	119
Fe_3O_4/ZnO/Ag	Methylene blue degradation; visible light 360 min; 20 W light	95%	120
Au/Ag/TNF	Methylene blue degradation; UV light 60 min; 12 W light	42%	121
Ag_3PO_4/TiO_2/Fe_3O_4	Orange 7 degradation; 405 nm light 60 min; 0.5 mg per mL catalyst	90%	122
Urchin-like Fe_3O_4/TiO_2	Ampicillin degradation; UV light 360 min; 8 W light	100%	123
TiO_2/Fe^{2+}/H_2O_2	Hospital wastewater COD degradation; solar light; pH: 7; 0.2 g per L TiO_2; 0.5 g per L Fe^{2+}; 1.35 g per L H_2O_2	99%	124
TiO_2/Fe_2O_3/CeO_2	NBB degradation; sol gel method; UV light 330 min; pH 3; 100 W light; 50 mg per L dye	89%	This work

dosage, and degradation duration were considered. The findings suggest that the photocatalytic efficiency of TFC, along with its stable reusability as mentioned earlier, is comparable to or better than most reported photocatalysts listed in Table 5. This indicates that TFC holds promise as a highly effective, easily separable, and stable photocatalyst, with significant potential for environmental cleanup due to its straightforward application.

4. Conclusion and future perspective

The co-doping strategy utilizing Ce and Fe achieved a significant enhancement in degradation efficiency (~89%), surpassing many previously reported TiO_2-based systems, and offers a scalable path for textile wastewater remediation. The investigation revealed that the TFC variant exhibited superior performance compared to others, with the performance order being TFC > TFCA > TFA > TF > T. The photocatalysts' estimated bandgap energies (E_g) were 2.9 eV for T, 2.8 eV for TF, 2.6 eV for TFC, 2.65 eV for TFA, and 2.35 eV for TFCA. Doped nanocatalysts exhibited lower E_g values due to dopants CeO_2 and Ag_2O, enhancing visible light absorption *via* surface plasmon resonance (SPR) and suppressing charge separation, thus facilitating easier e^-/h^+ pair formation. Conduction and valence band potentials were also computed. In most cases, the degradation pattern followed the pseudo-second order kinetics, displaying initial high degradation rates followed by a decrease until reaching a plateau around 210 min of degradation. XRD characterization confirmed the synthesis of anatase TiO_2 nanoparticles with a crystalline size of 13.32 nm, while TiO_2-based particles ranged from 5–7 nm. Lattice distortion, interface tension, and stress field reduced the crystalline size. SEM analysis revealed nanophotocatalyst agglomeration, though less common in co-doped TiO_2 nanocomposites due to longer stirring times. FTIR studies confirmed the formation of TiO_2 nanophotocatalysts.

Beyond the current findings, future studies could explore novel doping strategies or combinations to enhance visible light absorption further and charge separation efficiency. Additionally, investigating different synthesis methods or surface modifications may offer opportunities to tailor the catalytic properties and improve overall performance. Future studies should include intermediate compounds identification using GC-MS to confirm the proposed degradation pathway. Exploring the potential of immobilizing the catalysts could reduce catalyst loss and facilitate continuous operation in industrial settings.

Broader concentration variations might result in deeper insight into catalyst performance under extreme pollutant

Open Access Article. Published on 17 July 2025. Downloaded on 2/10/2026 5:25:23 PM. This article is licensed under a Creative Commons Attribution-NonCommercial 3.0 Unported Licence.

loads. Future studies will explore a wider concentration range to assess catalytic efficiency, saturation behavior, and rate limitations more comprehensively. In addition, the current study was conducted in controlled aqueous systems without the presence of common coexisting ions found in real wastewater. It is well-documented that anions such as Cl^-, NO_3^-, and SO_4^{2-} or cations like Ca^{2+} and Mg^{2+} may influence the photocatalytic process by scavenging reactive species or competing for active sites.[125] Therefore, evaluating the impact of these interfering species will be a key focus of our future work to ensure applicability in real-world scenarios.

Furthermore, developing efficient catalyst recovery and recycling methods would contribute to the sustainability of the process and reduce environmental impact. Regarding scalability, transitioning from lab-scale studies to solar irradiation for catalytic processes could significantly advance the field towards sustainable and practical applications. Research focusing on reactor design optimization for solar-driven processes could pave the way for a large-scale implementation and commercialization. Overall, future studies should aim to address critical challenges such as catalyst stability, scalability, and environmental impact to realize the full potential of TiO_2-based nanocatalysts in wastewater treatment and other applications.

Data availability

Data generated in the laboratory were used in the manuscript and additional data are presented in the ESI.†

Author contributions

Md. Burhan Kabir Suhan: writing – methodology, data collection, data analysis and original draft; Md. Khairul Bahar: writing – data analysis and original draft; Md. Shahinoor Islam: conceptualization, review & editing, supervision.

Conflicts of interest

The authors state that none of the work described in this study may have been influenced by any known conflicting financial interests or personal ties.

Acknowledgements

The authors express gratitude to the Department of Chemical Engineering at BUET for providing the laboratory facilities required for conducting the experiments and sample analysis, as well as to BUET CASR and BUET Chemical Engineering Forum (BCEF) for providing financial support for the study.

References

1 H. Karimi-Maleh, A. Ayati, S. Ghanbari, Y. Orooji, B. Tanhaei, F. Karimi, M. Alizadeh, J. Rouhi, L. Fu and M. Sillanpää, *J. Mol. Liq.*, 2021, **329**, 115062.
2 M. B. K. Suhan, S. B. Shuchi, M. R. Al-Mamun, H. Roy and M. S. Islam, *Environ. Nanotechnol., Monit. Manage.*, 2023, **19**, 100768.
3 Z. Abid, Z. Sarwar, N. Munir and S. Z. Safi, in *Enzymes in Textile Processing: A Climate Changes Mitigation Approach*, ed. M. Arshad, Springer Nature, Singapore, 2025, pp. 363–390.
4 W. Shi, Y. Zhao, Z. Li, W. Zhang, T. Zhou and K. Lin, *Chemosphere*, 2023, **338**, 139579.
5 A. Khan, A. Roy, S. Bhasin, T. Bin Emran, A. Khusro, A. Eftekhari, O. Moradi, H. Rokni and F. Karimi, *Food Chem. Toxicol.*, 2022, **164**, 112996.
6 A. Tkaczyk, K. Mitrowska and A. Posyniak, *Sci. Total Environ.*, 2020, **717**, 137222.
7 R. Kant, *Nat. Sci.*, 2012, **04**, 22–26.
8 S. Meddah, I. Djeghader, M. El, H. Samar and F. Ismail, *J. Appl. Res. Water Wastewater*, 2021, **8**, 133–139.
9 F. Hassan, B. Talami, A. Almansba, P. Bonnet, C. Caperaa, S. Dalhatou, A. Kane and H. Zeghioud, *ChemEngineering*, 2024, **8**, 50.
10 M. Rahmayanti, I. Nurhikmah and F. Larasati, *Molekul*, 2021, **16**, 67.
11 S. Ltaief, M. Jabli and S. Ben Abdessalem, *Carbohydr. Polym.*, 2021, **261**, 117908.
12 G. Crini and E. Lichtfouse, *Environ. Chem. Lett.*, 2019, **17**, 145–155.
13 G. Crini and E. Lichtfouse, in *Green Adsorbents for Pollutant Removal*, ed. G. Crini and E. Lichtfouse, Springer, Cham, 2018, pp. 1–21.
14 M. T. Yagub, T. K. Sen, S. Afroze and H. M. Ang, *Adv. Colloid Interface Sci.*, 2014, **209**, 172–184.
15 S. Hube, M. Eskafi, K. F. Hrafnkelsdóttir, B. Bjarnadóttir, M. Á. Bjarnadóttir, S. Axelsdóttir and B. Wu, *Sci. Total Environ.*, 2020, **710**, 136375.
16 P. Sanchis-Perucho, D. Aguado, J. Ferrer, A. Seco and Á. Robles, *Environ. Technol. Innovation*, 2024, **35**, 103732.
17 Y. Deng and R. Zhao, *Curr. Pollut. Rep.*, 2015, **1**, 167–176.
18 C. Dong, W. Fang, Q. Yi and J. Zhang, *Chemosphere*, 2022, **308**, 136205.
19 M. B. K. Suhan, M. R. Al-Mamun, N. Farzana, S. M. Aishee, M. S. Islam, H. M. Marwani, M. M. Hasan, A. M. Asiri, M. M. Rahman, A. Islam and M. R. Awual, *Nano-Struct. Nano-Objects*, 2023, **36**, 101050.
20 C. Wei, F. Zhang, Y. Hu, C. Feng and H. Wu, *Rev. Chem. Eng.*, 2017, **33**, 49–89.
21 M. Usman, K. Hanna and S. Haderlein, *Sci. Total Environ.*, 2016, **569–570**, 179–190.
22 P. Karuppasamy, N. Ramzan Nilofar Nisha, A. Pugazhendhi, S. Kandasamy and S. Pitchaimuthu, *J. Environ. Chem. Eng.*, 2021, **9**, 105254.
23 S. Stojadinović, N. Radić, R. Vasilić, N. Tadić and A. Tsanev, *Solid State Sci.*, 2022, **129**, 106896.
24 A. Mikolajczyk, E. Wyrzykowska, P. Mazierski, T. Grzyb, Z. Wei, E. Kowalska, P. N. A. Caicedo, A. Zaleska-Medynska, T. Puzyn and J. Nadolna, *Appl. Catal., B*, 2024, **346**, 123744.

© 2025 The Author(s). Published by the Royal Society of Chemistry

Open Access Article. Published on 17 July 2025. Downloaded on 2/10/2026 5:25:23 PM. This article is licensed under a Creative Commons Attribution-NonCommercial 3.0 Unported Licence.

25 F. G. Svensson, B. Cojocaru, Z. Qiu, V. Parvulescu, T. Edvinsson, G. A. Seisenbaeva, C. Tiseanu and V. G. Kessler, *Inorg. Chem.*, 2021, **60**, 14820–14830.
26 P. Akhter, A. Arshad, A. Saleem and M. Hussain, *Catalysts*, 2022, **12**, 1331.
27 N. R. Reddy, P. M. Reddy, N. Jyothi, A. S. Kumar, J. H. Jung and S. W. Joo, *J. Alloys Compd.*, 2023, **935**, 167713.
28 Z. Shayegan, F. Haghighat and C.-S. Lee, *J. Clean. Prod.*, 2021, **287**, 125462.
29 H. Khan and I. K. Swati, *Ind. Eng. Chem. Res.*, 2016, **55**, 6619–6633.
30 M. Z. Shahid, R. Mehmood, M. Athar, J. Hussain, Y. Wei and A. Khaliq, *ACS Appl. Nano Mater.*, 2021, **4**, 746–758.
31 Y. Zhang and Q. Li, *Solid State Sci.*, 2013, **16**, 16–20.
32 Z. Xia, S. Xing, H. Wang, D. Zhao, S. Wu, W. Jiang, N. Wang, S. Liu, C. Liu, W. Ding and Z. Zhang, *Opt. Mater.*, 2022, **129**, 112522.
33 N. Amo and S. J. Dhoble, in *Cerium-Based Materials: Synthesis, Properties and Applications*, Bentham Science Publishers, Sharjah, UAE, 2023, pp. 70–91.
34 M. G. Bhosale, R. S. Sutar, S. S. Londhe and M. K. Patil, *Appl. Organomet. Chem.*, 2022, **36**, 6586.
35 N. Ramesh, C. W. Lai, M. R. Bin Johan, S. M. Mousavi, I. A. Badruddin, A. Kumar, G. Sharma and F. Gapsari, *Heliyon*, 2024, **10**, e40998.
36 R. Acharya, B. Naik and K. Parida, in *Advanced Textile Engineering Materials*, ed. S. Ul-Islam and B. S. Butola, Wiley, Hoboken, NJ, 2018, pp. 389–418.
37 A. M. Dimiev and J. M. Tour, *ACS Nano*, 2014, **8**, 3060–3068.
38 D. E. Juárez-Cortazar, J. G. Torres-Torres, A. Hernandez-Ramirez, J. C. Arévalo-Pérez, A. Cervantes-Uribe, S. Godavarthi, A. E. E. de los Monteros, A. A. Silahua-Pavón and A. Cordero-Garcia, *Water*, 2022, **14**, 1389.
39 Y. Wei, Y. Huang, Y. Fang, Y. Zhao, D. Luo, Q. Guo, L. Fan and J. Wu, *Mater. Res. Bull.*, 2019, **119**, 110571.
40 S. B. Shuchi, M. B. K. Suhan, S. Bin Humayun, M. E. Haque and M. S. Islam, *J. Water Process Eng.*, 2021, **39**, 101690.
41 E. K. Maher, K. N. O'Malley, J. Heffron, J. Huo, B. K. Mayer, Y. Wang and P. J. McNamara, *Chemosphere*, 2019, **220**, 1141–1149.
42 M. B. K. Suhan, S. B. Shuchi, A. Anis, Z. Haque and M. S. Islam, *Environ. Nanotechnol., Monit. Manage.*, 2020, **14**, 100335.
43 M. M. Ba-abbad, A. A. H. Kadhum, A. B. Mohamad and M. S. Takriff, *Int. J. Electrochem. Sci.*, 2012, **7**, 4871–4888.
44 A. León, P. Reuquen, C. Garín, R. Segura, P. Vargas, P. Zapata and P. A. Orihuela, *Appl. Sci.*, 2017, **7**, 1–9.
45 M. Al-Amin, S. Chandra Dey, T. U. Rashid, M. Ashaduzzaman and S. M. Shamsuddin, *Int. Lett. Chem. Phys. Astron.*, 2016, **2**, 14–21.
46 M. R. Al-Mamun, S. Kader and M. S. Islam, *Environ. Nanotechnol., Monit. Manage.*, 2021, **16**, 100514.
47 X. Lu, X. Lv, Z. Sun and Y. Zheng, *Eur. Polym. J.*, 2008, **44**, 2476–2481.
48 D. N. Kendall, *Anal. Chem.*, 1953, **25**, 382–389.
49 G. V. Jere and C. C. Patel, *Can. J. Chem.*, 1962, **40**, 1576–1578.
50 A. M. Bobrova, I. G. Zhigun, M. I. Bragina and A. A. Fotiev, *J. Appl. Spectrosc.*, 1968, **8**, 59–63.
51 K. L. A. Chan and S. G. Kazarian, *Analyst*, 2006, **131**, 126–131.
52 F. Yang, M. Zhao, B. Zheng, D. Xiao, L. Wu and Y. Guo, *J. Mater. Chem.*, 2012, **22**, 25471.
53 S. Bai, H. Liu, J. Sun, Y. Tian, S. Chen, J. Song, R. Luo, D. Li, A. Chen and C. C. Liu, *Appl. Surf. Sci.*, 2015, **338**, 61–68.
54 H. Wang, J. Li, X. Quan and Y. Wu, *Appl. Catal. B Environ.*, 2008, **83**, 72–77.
55 T. U. Rahman, H. Roy, A. Z. Shoronika, A. Fariha, M. Hasan, M. S. Islam, H. M. Marwani, A. Islam, M. M. Hasan, A. K. D. Alsukaibi, M. M. Rahman and M. R. Awual, *J. Mol. Liq.*, 2023, **338**, 122764.
56 C. Girginov, P. Stefchev, P. Vitanov and H. Dikov, *J. Eng. Sci. Technol. Rev.*, 2012, **5**, 14–17.
57 A. Rey, P. García-Muñoz, M. D. Hernández-Alonso, E. Mena, S. García-Rodríguez and F. J. Beltrán, *Appl. Catal., B*, 2014, **154–155**, 274–284.
58 C. M. Magdalane, G. M. A. Priyadharsini, K. Kaviyarasu, A. I. Jothi and G. G. Simiyon, *Surf. Interfaces*, 2021, **25**, 101296.
59 İ. Ç. Davaslıoğlu, K. Volkan Özdokur, S. Koçak, Ç. Çırak, B. Çağlar, B. B. Çırak and F. Nil Ertaş, *J. Mol. Struct.*, 2021, **1241**, 130673.
60 L. Pirinejad, A. Maleki, B. Shahmoradi, H. Daraei, J. K. Yang and S. M. Lee, *J. Mol. Liq.*, 2019, **279**, 232–240.
61 M. Sahadat Hossain and S. Ahmed, *Results Mater.*, 2023, **20**, 100492.
62 S. Chalotra, S. Kaur, Kriti, P. Kaur, P. Kaur, P. Kaur and D. P. Singh, *Phase Transitions*, 2023, **96**, 528–546.
63 T. van Westen and R. D. Groot, *Cryst. Growth Des.*, 2018, **18**, 4952–4962.
64 R. S. Dubey, H. M. Pathan, B. B. Kale and J. D. Ambekar, *Micro Nano Lett.*, 2020, **15**, 1120–1125.
65 H. Sun, B. Dong, G. Su, R. Gao, W. Liu, L. Song and L. Cao, *Appl. Surf. Sci.*, 2015, **343**, 181–187.
66 Y. Wu, Y. Dong, X. Xia, X. Liu and H. Li, *Appl. Surf. Sci.*, 2016, **364**, 829–836.
67 M. Rashid Al-Mamun, K. T. Hossain, S. Mondal, M. Afroza Khatun, M. Shahinoor Islam and D. M. Zaved Hossain Khan, *S. Afr. J. Chem. Eng.*, 2022, **40**, 113–125.
68 R. A. Spurr and H. Myers, *Anal. Chem.*, 1957, **29**, 760–762.
69 Z. Abbas, J. P. Holmberg, A. K. Hellström, M. Hagström, J. Bergenholtz, M. Hassellöv and E. Ahlberg, *Colloids Surf., A*, 2011, **384**, 254–261.
70 M. A. Mahadadalkar, N. Park, M. Yusuf, S. Nagappan, M. Nallal and K. H. Park, *Chemosphere*, 2023, **330**, 138599.
71 K. Wu, Z. Shi, X. Wang and J. Wang, *Crystals*, 2022, **12**, 1094.
72 M. Hasan Khan Neon and M. S. Islam, *Environ. Nanotechnol., Monit. Manage.*, 2019, **12**, 100244.
73 G. Li, L. Lv, H. Fan, J. Ma, Y. Li, Y. Wan and X. S. Zhao, *J. Colloid Interface Sci.*, 2010, **348**, 342–347.
74 D. Zhou, Z. Ji, X. Jiang, D. R. Dunphy, J. Brinker and A. A. Keller, *PLoS One*, 2013, **8**, 1–7.
75 M. D. Nasikhudin, A. Kusumaatmaja and K. Triyana, *J. Phys.:Conf. Ser.*, 2018, **1011**, 012069.

© 2025 The Author(s). Published by the Royal Society of Chemistry

Open Access Article. Published on 17 July 2025. Downloaded on 2/10/2026 5:25:23 PM. This article is licensed under a Creative Commons Attribution-NonCommercial 3.0 Unported Licence.

76 M. R. Al-Mamun, S. Kader, M. S. Islam and M. Z. H. Khan, *J. Environ. Chem. Eng.*, 2019, **7**, 103248.
77 M. Zhang, N. Han, Y. Fei, J. Liu, L. Xing, A. Núñez-Delgado, M. Jiang and S. Liu, *J. Environ. Manage.*, 2021, **297**, 113311.
78 H. Khan, Z. Jiang and D. Berk, *Sol. Energy*, 2018, **162**, 420–430.
79 D. Zhao, X. Yang, C. Chen and X. Wang, *J. Colloid Interface Sci.*, 2013, **398**, 234–239.
80 M. Jahdi, E. N. Nxumalo, S. D. Mhlanga, M. Orlandi and A. Miotello, *Mater. Sci. Semicond. Process.*, 2023, **157**, 107305.
81 P. R. Jubu, O. S. Obaseki, D. I. Ajayi, E. Danladi, K. M. Chahrour, A. Muhammad, S. Landi, T. Igbawua, H. F. Chahul and F. K. Yam, *J. Opt.*, 2024, **53**, 5054–5064.
82 S. Ghattavi and A. Nezamzadeh-Ejhieh, *Desalin. Water Treat.*, 2019, **166**, 92–104.
83 N. Omrani and A. Nezamzadeh-Ejhieh, *Sep. Purif. Technol.*, 2020, **235**, 116228.
84 T. Chankhanittha, V. Somaudon, J. Watcharakitti and S. Nanan, *J. Mater. Sci.: Mater. Electron.*, 2021, **32**, 1977–1991.
85 S. Xiong, X. Liu, X. Zhu, G. Liang, Z. Jiang, B. Cui and J. Bai, *Ecotoxicol. Environ. Saf.*, 2021, **208**, 111519.
86 L. Huang and H. Lu, *Phys. Rev. B: Condens. Matter Mater. Phys.*, 2019, **99**, 045122.
87 M. Rahm, T. Zeng and R. Hoffmann, *J. Am. Chem. Soc.*, 2019, **141**, 342–351.
88 H. Ali, T. M. Tiama and A. M. Ismail, *Int. J. Biol. Macromol.*, 2021, **186**, 278–288.
89 F. Maleki, G. Di Liberto and G. Pacchioni, *ACS Appl. Mater. Interfaces*, 2023, **15**, 11216–11224.
90 L. A. García Rodenas, A. D. Weisz, G. E. Magaz and M. A. Blesa, *J. Colloid Interface Sci.*, 2000, **230**, 181–185.
91 J. E. Duffy, M. A. Anderson, C. G. Hill and W. A. Zeltner, *Ind. Eng. Chem. Res.*, 2000, **39**, 3698–3706.
92 X. Shen, in *Molecularly Imprinted Catalysts*, Elsevier, Amsterdam, 2016, pp. 211–228.
93 T. Mahmood, M. T. Saddique, A. Naeem, P. Westerhoff, S. Mustafa and A. Alum, *Ind. Eng. Chem. Res.*, 2011, **50**, 10017–10023.
94 S. Kader, M. R. Al-Mamun, M. B. K. Suhan, S. B. Shuchi and M. S. Islam, *Environ. Technol. Innovation*, 2022, **27**, 102476.
95 Y. Liu, C. Zhao, B. Sun, H. Zhu, W. Xu and Z. Yang, *Mol. Catal.*, 2024, **560**, 114095.
96 K. Solymos, I. Babcsányi, B. Ariya, T. Gyulavári, Á. Ágoston, Á. Szamosvölgyi, Á. Kukovecz, Z. Kónya, A. Farsang and Z. Pap, *Environ. Sci.: Nano*, 2024, **11**, 1204–1216.
97 A. Fallah Shojaei, A. Shams-Nateri and M. Ghomashpasand, *Superlattices Microstruct.*, 2015, **88**, 211–224.
98 H. D. Tran, D. Q. Nguyen, P. T. Do and U. N. P. Tran, *RSC Adv.*, 2023, **13**, 16915–16925.
99 H. N. Tran, *Water*, 2023, **15**, 1231.
100 J. A. Pinedo-Escobar, J. Fan, E. Moctezuma, C. Gomez-Solís, C. J. Carrillo Martinez and E. Gracia-Espino, *ACS Omega*, 2021, **6**, 11840–11848.
101 Z. Wang, Z. Lin, S. Shen, W. Zhong and S. Cao, *Chin. J. Catal.*, 2021, **42**, 710–730.
102 M. R. Al-Mamun, M. N. Karim, N. A. Nitun, S. Kader, M. S. Islam and M. Z. H. Khan, *Environ. Technol. Innovation*, 2021, **22**, 101537.
103 I. K. Konstantinou and T. A. Albanis, *Appl. Catal., B*, 2004, **49**, 1–14.
104 K. Sivula, F. Le Formal and M. Grätzel, *ChemSusChem*, 2011, **4**, 432–449.
105 A. Trovarelli, *Catal. Rev.*, 1996, **38**, 439–520.
106 N. A. Ramos-Delgado, L. Hinojosa-Reyes, I. L. Guzman-Mar, M. A. Gracia-Pinilla and A. Hernández-Ramírez, *Catal. Today*, 2013, **209**, 35–40.
107 M. V. Dozzi, C. D'Andrea, B. Ohtani, G. Valentini and E. Selli, *J. Phys. Chem. C*, 2013, **117**, 25586–25595.
108 T. Luttrell, S. Halpegamage, J. Tao, A. Kramer, E. Sutter and M. Batzill, *Sci. Rep.*, 2015, **4**, 4043.
109 S. Sood, A. Umar, S. K. Mehta and S. K. Kansal, *J. Colloid Interface Sci.*, 2015, **450**, 213–223.
110 C. Thambiliyagodage and L. Usgodaarachchi, *Curr. Res. Green Sustainable Chem.*, 2021, **4**, 100186.
111 C. Lu, Y. Chen, H. Zhang, L. Tang, S. Wei, Y. Song and J. Wang, *Res. Chem. Intermed.*, 2016, **42**, 4651–4668.
112 V. Vaiano, O. Sacco, D. Sannino, M. Stoller, P. Ciambelli and A. Chianese, *Chem. Eng. Trans.*, 2016, **47**, 235–240.
113 R. G. Ciocarlan, E. M. Seftel, M. Mertens, A. Pui, M. Mazaj, N. Novak Tusar and P. Cool, *Mater. Sci. Eng., B*, 2018, **230**, 1–7.
114 X. Yan, K. Yuan, N. Lu, H. Xu, S. Zhang, N. Takeuchi, H. Kobayashi and R. Li, *Appl. Catal., B*, 2017, **218**, 20–31.
115 A. Hafeez, N. Shezad, F. Javed, T. Fazal, M. Saif ur Rehman and F. Rehman, *Sep. Purif. Technol.*, 2021, **269**, 118728.
116 E. Ahmadi, B. Shokri, A. Mesdaghinia, R. Nabizadeh, M. Reza Khani, S. Yousefzadeh, M. Salehi and K. Yaghmaeian, *Sep. Purif. Technol.*, 2020, **250**, 117185.
117 A. A. Isari, A. Payan, M. Fattahi, S. Jorfi and B. Kakavandi, *Appl. Surf. Sci.*, 2018, **462**, 549–564.
118 M. Amoli-Diva, A. Anvari and R. Sadighi-Bonabi, *Ceram. Int.*, 2019, **45**, 17837–17846.
119 P. Zhang, Z. Mo, L. Han, X. Zhu, B. Wang and C. Zhang, *Ind. Eng. Chem. Res.*, 2014, **53**, 8057–8061.
120 S. Chidambaram, B. Pari, N. Kasi and S. Muthusamy, *J. Alloys Compd.*, 2016, **665**, 404–410.
121 M. Misra, N. Singh and R. K. Gupta, *Catal. Sci. Technol.*, 2017, **7**, 570–580.
122 J.-W. Xu, Z.-D. Gao, K. Han, Y. Liu and Y.-Y. Song, *ACS Appl. Mater. Interfaces*, 2014, **6**, 15122–15131.
123 Y. Zhao, C. Tao, G. Xiao, G. Wei, L. Li, C. Liu and H. Su, *Nanoscale*, 2016, **8**, 5313–5326.
124 S. Adish Kumar, G. S. Sree Lekshmi, J. Rajesh Banu and I. Tae Yeom, *Water Qual. Res. J. Can.*, 2014, **49**, 223–233.
125 J. Wang and S. Wang, *Chem. Eng. J.*, 2021, **411**, 128392.

© 2025 The Author(s). Published by the Royal Society of Chemistry